Cycloidal spiral magnetic structures in the spin-chain compounds BaRFeO$_4$ (R = Yb and Tm): Ordered Yb versus partly ordered Tm

Andreas Dönni,[1] Vladimir Y. Pomjakushin,[2] Kazunari Yamaura,[1,3] and Alexei A. Belik[1,*]

[1]*International Center for Materials Nanoarchitectonics (WPI-MANA), National Institute for Materials Science (NIMS), Namiki 1-1, Tsukuba, Ibaraki 305-0044, Japan*

[2]*Laboratory for Neutron Scattering and Imaging (LNS), Paul Scherrer Institut, 5232 Villigen PSI, Switzerland*

[3]*Graduate School of Chemical Sciences and Engineering, Hokkaido University, North 10 West 8, Kita-ku, Sapporo, Hokkaido 060–0810, Japan*

(Received 12 February 2023; accepted 20 March 2023; published 11 April 2023)

BaRFeO$_4$ compounds containing magnetic rare-earth ions (R = Yb, Tm) were prepared by a conventional solid-state method in air. We present detailed measurements of magnetic properties (specific heat, magnetic susceptibility) to demonstrate the presence of three successive magnetic phase transitions (at T_{N1}, T_{N2}, and T_3) in both compounds and employed neutron diffraction to determine the magnetic structures. Both compounds are isostructural (orthorhombic space group *Pnma*) and magnetic ions form rings and chains along the b direction. All magnetic structures are incommensurate with a propagation vector $\mathbf{k} = (0,\ 0,\ k_z)$. Magnetic ordering of Fe^{3+} ions occurs at T_{N1} and T_{N2}, where two different irreducible representations (irreps) order. Below T_{N1}, there is a collinear spin-density wave with ordered Fe^{3+} moments along the chain direction (b axis). Below T_{N2}, this component remains stable and an additional component inside the ac plane appears. Each Fe chain adopts a collinear antiferromagnetic structure with a constant magnetic phase. The two Fe rings in the unit cell have a different chirality and a noncollinear coupling. The mixing of two irreps leads to a cycloidal spiral magnetic structure that allows spin-induced ferroelectric polarization at T_{N2}. With the presence of modulated components both perpendicular and along the propagation vector $\mathbf{k}$, the magnetic structure can be viewed as a sum of a helix and a cycloid structure. For BaTmFeO$_4$, the magnetic structure has a larger cycloidal contribution and the dielectric constant ε exhibits a small peak at T_{N2}. Yb^{3+} moments order at T_3 with each Yb chain having a constant magnetic phase and a collinear antiferromagnetic structure stabilized by $4f-4f$ electron-exchange interactions. In contrast, no constant magnetic phase is observed at the Tm chains. Below T_3, magnetic order of Tm2 ions is induced by $3d-4f$ electron-exchange interactions and Tm1 ions remain disordered down to the lowest measured temperature $T = 1.6$ K due to frustration of magnetic exchange interactions. The obtained magnetic structures are compared with those of BaYFeO$_4$.

DOI: 10.1103/PhysRevB.107.134412

I. INTRODUCTION

Information about magnetic structures (such as magnetic space group, propagation vectors, magnitude, and direction of spins at each site and their evolution with temperature) is essential for correct understanding and interpretation of macroscopic magnetic and sometimes dielectric/ferroelectric properties of materials [1]. For example, macroscopic negative magnetization phenomena, when magnetization decreases with decreasing temperature and becomes negative, are often connected to the presence of two (or several) magnetic sublattices, coupled antiferromagnetically and having nonequal ordered moments, and their different evolution with temperature [2–4]. In type-II multiferroics, macroscopic ferroelectric polarization develops in otherwise centrosymmetric materials due to breaking the inversion symmetry by a magnetic order [1,5,6]. As a result, there are strong magnetoelectric couplings allowing the control of ferroelectric properties by a magnetic field and the control of magnetic properties by an electric field. Therefore, if a (sharp) dielectric constant anomaly appears at a magnetic transition temperature one should expect a polar magnetic space group for the underlying magnetic structure.

We have recently prepared a series of isostructural compounds with the chemical composition of BaRFeO$_4$ with R = Dy, Ho, Er, Tm, and Yb [7–9]. They are isostructural with BaYFeO$_4$ [10–14]. We found that they all showed different temperature dependences of dielectric constant and magnetization [7,8]. A very sharp (but weak) dielectric constant anomaly was observed in BaTmFeO$_4$ at $T_{N1} = 46$ K, while a much broader kinklike dielectric anomaly was found in BaYbFeO$_4$ at $T_{N2} = 36$ K. One magnetic transition was detected in BaTmFeO$_4$, while two well-separated magnetic transitions were found in BaYbFeO$_4$ (at $T_{N2} = 36$ K and $T_{N1} = 57$ K). BaRFeO$_4$ with R = Dy, Ho, and Er exhibit three magnetic transitions and more complex temperature dependences of dielectric constant [7,8,15].

In this work, we attempted to understand the differences between BaYbFeO$_4$ and BaTmFeO$_4$ through more detailed macroscopic measurements (specific heat and magnetic susceptibility) to clarify the number of magnetic phase transitions and through neutron diffraction to determine the magnetic structures. We found that both materials BaYbFeO$_4$ and BaTmFeO$_4$ actually undergo three magnetic phase transitions,

*Corresponding author: Alexei.Belik@nims.go.jp

similar to all other members of this series with magnetic rare-earth cations. For the isostructural compound $BaYFeO_4$ with two magnetic phase transitions and purely $3d$ electron magnetism, neutron-diffraction measurements determined a spin-density wave below $T_{N1} = 48$ K and an incommensurate cycloid below $T_{N2} = 36$ K [11]. Here, we extend the magnetic structure determination to $BaRFeO_4$ compounds with magnetic rare-earth elements (R = Yb, Tm) and coexisting $3d$ and $4f$ electron magnetism. We find complex low-symmetry incommensurate magnetic structures dominated by ordered Fe^{3+} ions at T_{N1} and T_{N2}. At the lowest measured temperature $T = 1.6$ K, the Yb sublattice is fully ordered, whereas the Tm sublattice remains partly ordered. $BaTmFeO_4$ has a larger component of ordered Fe^{3+} moments along the magnetic propagation vector that could explain the larger spin-induced electric polarization.

II. EXPERIMENT

Ferrite $BaRFeO_4$ samples with R = Yb and Tm (about 6 g each for neutron-diffraction measurements) were synthesized from stoichiometric mixtures of $BaCO_3$ (99.9%), Yb_2O_3 (99.9%), Tm_2O_3 (99.9%), and Fe_2O_3 (99.999%) using a conventional solid-state annealing method. The mixtures were pressed into pellets and annealed in air on Pt foil successively at 1430 K for 40 h + 1470 K for 35 h + 1510 K for 40 h ($BaYbFeO_4$), and at 1430 K for 36 h + 1430 K for 36 h + 1470 K for 58 h + 1510 K for 40 h ($BaTmFeO_4$) with grinding after each step (marked by +). The $BaTmFeO_4$ sample was single-phase based on laboratory x-ray diffraction, while small amounts of Yb_2O_3 and $BaFeO_{3-\delta}$ impurities could be detected by synchrotron x-ray diffraction in $BaYbFeO_4$ [8].

Magnetic property measurements were performed through the magnetic phase transitions. Specific-heat C_p data were collected on cooling at zero magnetic field by the pulse-relaxation method using a commercial calorimeter (Quantum Design PPMS). The magnetic susceptibility was measured by a superconducting quantum interference device magnetometer (Quantum Design, MPMS3) between 1.8 and 70 K using a 500-Oe magnetic field on cooling (FCC) and warming (FCW), where FC means field cooled.

Neutron powder diffraction (NPD) experiments were done at the Paul Scherrer Institute, Switzerland. $BaYbFeO_4$ and $BaTmFeO_4$ were measured at the high-resolution powder diffractometer for thermal neutrons (HRPT) [16] using an incident wavelength of 1.886 Å [obtained from a focusing Ge(511) monochromator] and no additional collimation. NPD data were collected in the magnetically ordered and paramagnetic states at temperatures between 1.6 and 70 K for a 2θ range of 3.55°–164.50° and a step width of 0.05°. The diffraction patterns were analysed by the Rietveld method using the FULLPROF SUITE [17]. The shapes of the Bragg peaks were refined using a Thompson-Cox-Hastings pseudo-Voigt function that consists of a Gaussian and a Lorentzian component. The correlation length (L) of the magnetic structure has been estimated from the Lorentzian peak broadening of the resolution parameter Y (Y_m of the magnetic structure compared to Y_n of the crystal structure), by using the well-known Debye-Scherrer formula $\sigma_1 = Y_m - Y_n = \lambda/L$ [18]. Here, λ = 1.886 Å is the neutron wavelength. Possible models for the magnetic structures were deducted based on a group-theory analysis using the programs ISODISTORT [19] and BASIREPS in the FULLPROF SUITE program package [17].

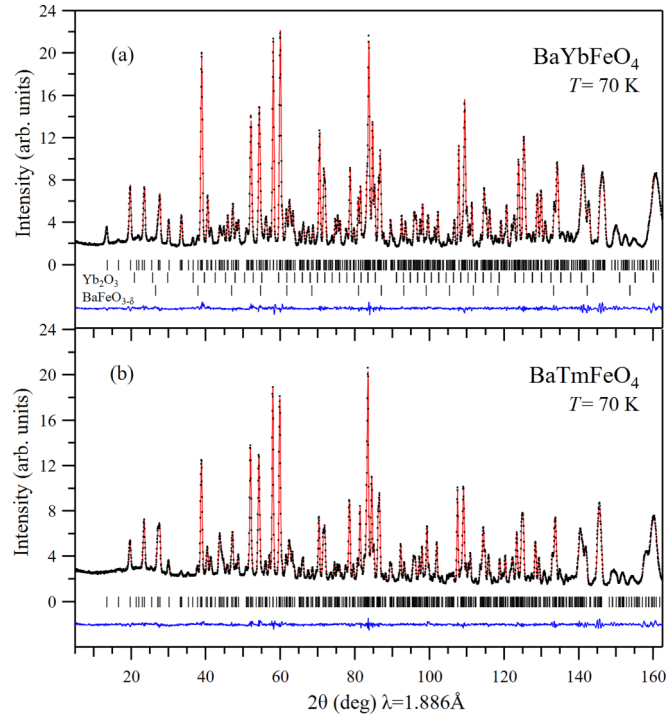

FIG. 1. Experimental (black dots), calculated (red line), and difference (blue line) neutron-diffraction patterns of $BaYbFeO_4$ (a) and $BaTmFeO_4$ (b) in the paramagnetic state at $T = 70$ K. Tick marks indicate Bragg peak positions. Small amounts of impurity phases Yb_2O_3 (1.0 wt. %) and $BaFeO_{3-\delta}$ (1.1 wt. %) are included in the refinement of $BaYbFeO_4$.

III. RESULTS AND DISCUSSION

A. Crystal structures and magnetic phase transitions

The crystal structures of $BaYbFeO_4$ and $BaTmFeO_4$ at room temperature have been determined by synchrotron x-ray diffraction [8]. Both compounds crystallize in the orthorhombic space group *Pnma* (No. 62) and are isostructural with $BaYFeO_4$ [10]. The refinement of the crystal structures of paramagnetic $BaYbFeO_4$ and $BaTmFeO_4$ at $T = 70$ K based on high-resolution NPD data is shown in Fig. 1. The resulting structural parameters are summarized in Table I. Selected bond lengths and bond-valence sums [20] are given in Tables S1 and S2 in the Supplemental Material [21]. The $BaTmFeO_4$ sample contained no detectable impurity phase, whereas for $BaYbFeO_4$, small amounts of impurity-phase contributions (Yb_2O_3, 1.0 wt. % and $BaFeO_{3-\delta}$, 1.1 wt. %) were included in the refinement. R_2O_3 (Yb_2O_3, cubic space group $Ia\bar{3}$, No. 206 with $a = 10.399$ Å at $T = 70$ K) and $BaFeO_{3-\delta}$ (cubic space group $Pm\bar{3}m$, No. 221, with $a = 4.107$ Å at $T = 70$ K) are common impurities for $BaRFeO_4$ materials and the synthesis method at ambient pressure [8]. The $BaYFeO_4$ structure type is formed for the compounds with R = Dy–Yb and Y. Among these materials, $BaYbFeO_4$ has the smallest and $BaTmFeO_4$ the second-smallest R^{3+} ionic radius.

TABLE I. Structure parameters of $BaYbFeO_4$ and $BaTmFeO_4$ at $T = 70$ K refined from powder neutron diffraction data (HRPT, $\lambda = 1.886$ Å). Space group *Pnma* (No. 62); $Z = 8$. WP: Wyckoff position. Occupation factor $g = 1$ for all the sites.

$BaYbFeO_4$, $T = 70$ K:
a= 13.0419(1) Å; b= 5.6493(1) Å; c= 10.1637(1) Å; $V = 748.84(1)$ Å^3.
χ^2= 3.32; $R_{wp} = 2.52\%$; R_{exp}= 1.38%; $R_{Bragg} = 1.45\%$.

Site	WP	x	y	z	B (Å^2)
Ba1	4c	0.209 7(2)	0.25	0.673 7(2)	= B(Yb1)
Ba2	4c	0.415 3(2)	0.25	0.395 4(2)	= B(Yb1)
Yb1	4c	0.415 43(7)	0.25	0.014 49(9)	0.09(1)
Yb2	4c	0.143 42(7)	0.25	0.309 88(9)	= B(Yb1)
Fe1	4c	0.468 60(9)	0.25	0.717 1(1)	0.08(2)
Fe2	4c	0.190 86(9)	0.25	0.023 3(1)	= B(Fe1)
O1	4c	0.586 3(2)	0.25	0.614 4(2)	0.35(1)
O2	4c	0.292 3(2)	0.25	0.181 6(2)	= B(O1)
O3	8d	0.005 6(1)	0.508 4(3)	0.360 6(1)	= B(O1)
O4	8d	0.216 5(1)	0.508 1(3)	0.440 5(1)	= B(O1)
O5	8d	0.112 4(1)	1.000 5(3)	0.133 6(1)	= B(O1)

$BaTmFeO_4$, $T = 70$ K:
a= 13.0728(1) Å; b= 5.6618(1) Å; c= 10.1747(1) Å; $V = 753.09(1)$ Å^3.
χ^2= 2.79; $R_{wp} = 2.43\%$; R_{exp}= 1.45%; $R_{Bragg} = 1.62\%$.

Site	WP	x	y	z	B (Å^2)
Ba1	4c	0.209 9(2)	0.25	0.674 0(2)	= B(Tm1)
Ba2	4c	0.415 0(2)	0.25	0.394 9(2)	= B(Tm1)
Tm1	4c	0.414 6(1)	0.25	0.014 8(2)	0.05(1)
Tm2	4c	0.142 9(1)	0.25	0.310 8(2)	= B(Tm1)
Fe1	4c	0.468 68(9)	0.25	0.716 5(1)	0.11(1)
Fe2	4c	0.189 94(9)	0.25	0.023 5(1)	= B(Fe1)
O1	4c	0.586 4(2)	0.25	0.614 5(2)	0.29(1)
O2	4c	0.292 3(2)	0.25	0.181 7(2)	= B(O1)
O3	8d	0.005 7(1)	0.508 3(3)	0.360 4(1)	= B(O1)
O4	8d	0.217 41(9)	0.508 0(3)	0.440 4(1)	= B(O1)
O5	8d	0.112 12(8)	0.999 7(3)	0.132 2(1)	= B(O1)

The crystal structure of BaRFeO$_4$ (R = Yb, Tm) contains magnetic atoms Fe1, Fe2, R1, and R2, all located on 4c sites (x, 1/4, z), and the structure parameters are given in Table I. The arrangement of the magnetic ions in the crystal structure is illustrated in Fig. 2. There are rings consisting of 4 magnetic ions, for example, Fe1$_1$, Fe2$_2$, Fe1$_3$, and Fe2$_4$. Each ring forms a chain propagating along the b axis. The chains of Fe^{3+} ions are built by alternate corner shared units of $[FeO_5]^{7-}$ square pyramids (Fe1) and $[FeO_6]^{9-}$ octahedra (Fe2) [10]. All magnetic ions are part of rings and chains. The crystallographic unit cell contains two rings formed by Fe^{3+} and two by R^{3+} ions [see Fig. 2(b)]. Selected distances between magnetic ions at $T = 70$ K are given in Table II for $BaTmFeO_4$ and in Table S3 [21] for $BaYbFeO_4$. The distances are similar in both compounds. For $BaTmFeO_4$, Fe–Fe distances inside the chains are 3.786(2) Å (for Fe1$_1$–Fe2$_2$, nearest neighbor, 1x) and 4.021(1) Å (for Fe1$_1$–Fe2$_4$, next-nearest neighbor, 2x). They are significantly shorter than all other Fe–Fe distances of at least 4.8 Å (interchain) and 5.3 Å (intrachain). The third-nearest neighbor of Fe1$_1$ is Fe2$_1$ at 4.800(2) Å (interchain, 1x) and the fourth-nearest neighbor is Fe1$_3$ at 5.301(2) Å (intrachain, 2x).

Figure 3 compares temperature-dependent magnetic property measurements (specific heat C_p/T, inverse magnetic susceptibility χ^{-1}, and dielectric constant ε) for $BaYbFeO_4$ (a) and $BaTmFeO_4$ (b), (c). The data for ε shown in Fig. 3(c) have been published in Ref. [8]. Figure S1 [21] compares the temperature dependence of the magnetic susceptibility χ and the differential $d(\chi T)/dT$ for $BaYbFeO_4$ and $BaTmFeO_4$, measured at a magnetic field of 500 Oe for warming (FCW) and cooling (FCC). $d(\chi T)/dT$ data measured for FCW and FCC show a small hysteresis, particularly near T_{N2}. Specific heat and magnetic susceptibility have been measured on the samples used for the neutron-diffraction experiments. The results displayed in Figs. 3 and S1 [21] suggest the presence of three magnetic phase transitions in both compounds, $BaYbFeO_4$ (at $T_{N1} = 57$ K, $T_{N2} = 34$ K, and $T_3 \approx 18$ K) and $BaTmFeO_4$ (at $T_{N1} = 47.5$ K, $T_{N2} = 46$ K, and $T_3 \approx 6$ K). Based on magnetic susceptibility and dielectric constant measurements, in the previous work [8], only two and one magnetic phase transitions have been detected for $BaYbFeO_4$ and $BaTmFeO_4$, respectively. Neutron-diffraction data presented in this work confirm that T_{N1} and T_{N2} correspond to magnetic ordering transitions of Fe^{3+} moments, whereas T_3 is connected to the appearance of ordered rare-earth moments. T_{N1} and T_{N2} are detected by anomalies in the differential $d(\chi T)/dT$ versus T curves and no clear anomalies are observed in the C_p/T curves. Similar results have been

TABLE II. Selected distances between magnetic ions in $BaTmFeO_4$ at $T = 70$ K.

Distances inside Fe ring:		Distances inside Tm ring:	
$Fe1_1$ - $Fe2_2$ (1x)	3.786(2) Å	$Tm1_1$ - $Tm2_2$ (1x)	3.473(2) Å
$Fe1_1$ - $Fe2_4$ (2x)	4.021(1) Å	$Tm1_1$ - $Tm2_4$ (2x)	3.590(2) Å
$Fe1_1$ - $Fe1_3$ (2x)	5.301(2) Å	$Tm1_1$ - $Tm1_3$ (2x)	3.618(1) Å
$Fe2_2$ - $Fe2_4$ (2x)	5.736(1) Å	$Tm2_2$ - $Tm2_4$ (2x)	6.067(2) Å
Distances from $Fe1_1$ to Tm:		Distances from $Fe2_2$ to Tm:	
$Fe1_1$ - $Tm1_1$ (1x)	3.116(2) Å	$Fe2_2$ - $Tm1_2$ (1x)	2.938(2) Å
$Fe1_1$ - $Tm2_4$ (2x)	3.326(1) Å	$Fe2_2$ - $Tm2_2$ (1x)	2.987(2) Å
$Fe1_1$ - $Tm1_3$ (2x)	4.221(2) Å	$Fe2_2$ - $Tm2_3$ (2x)	4.180(2) Å
Distances from $Fe1_3$ to Tm:		Distances from $Fe2_4$ to Tm:	
$Fe1_3$ - $Tm1_3$ (1x)	3.116(2) Å	$Fe2_4$ - $Tm1_4$ (1x)	2.938(2) Å
$Fe1_3$ - $Tm2_2$ (2x)	3.326(1) Å	$Fe2_4$ - $Tm2_4$ (1x)	2.987(2) Å
$Fe1_3$ - $Tm1_1$ (2x)	4.221(2) Å	$Fe2_4$ - $Tm2_1$ (2x)	4.180(2) Å

reported for $BaYFeO_4$ [10] and $BaDyFeO_4$ [7]. The release of magnetic entropy at T_{N1} and T_{N2} is very small. At lower temperature, T_3 is detected by an increase of C_p/T values. According to an anomaly in the C_p/T curve of $BaYbFeO_4$, ordered Yb^{3+} moments appear at $T_3 \approx 18$ K and reach saturation at around 10 K. In $BaTmFeO_4$, a strong increase of C_p/T

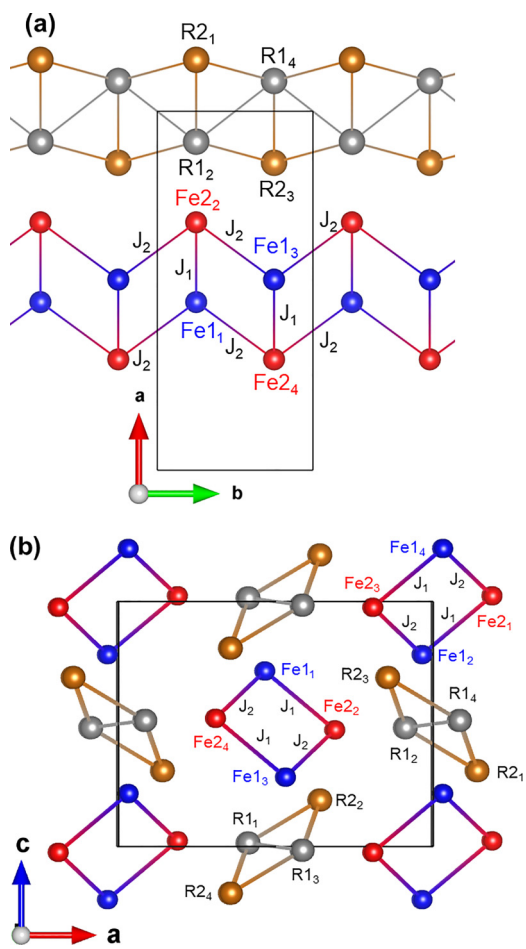

FIG. 2. Arrangement of magnetic Fe^{3+} and R^{3+} ions (R = Yb, Tm) in the crystal structure. Rings and the chains propagating along the b axis are shown as a projection onto the ab plane (a) and ac plane (b). Drawings were made using the program VESTA [22].

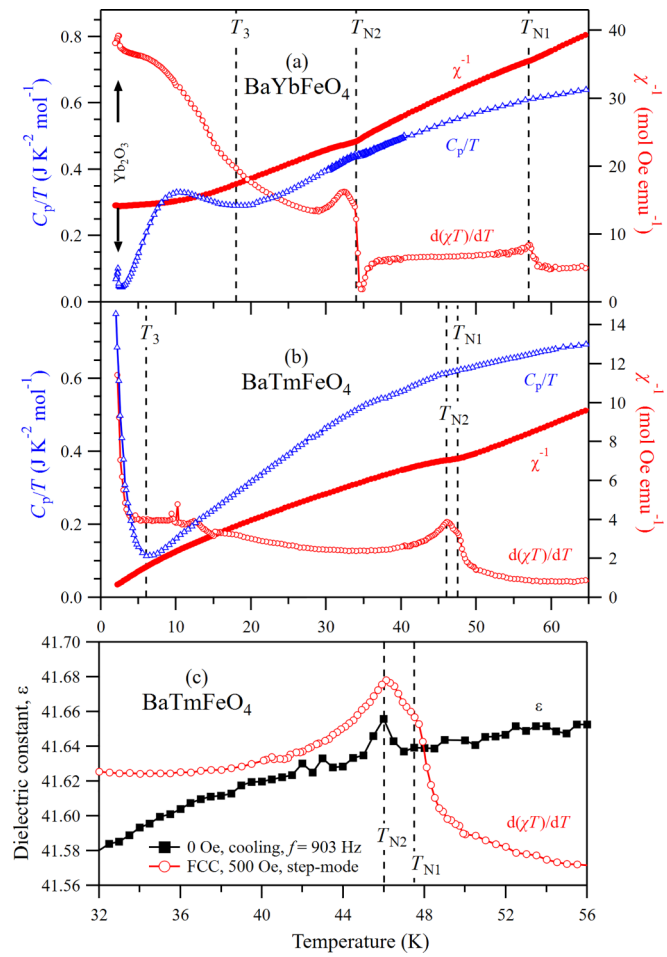

FIG. 3. Temperature dependence of the specific heat C_p/T (measured on cooling at zero field), the magnetic susceptibility χ^{-1} (measured on cooling at a magnetic field of 500 Oe), and the differential $d(\chi T)/dT$ (in arbitrary units) for (a) $BaYbFeO_4$ and (b) $BaTmMnO_4$. Vertical dashed lines indicate magnetic phase transitions at T_{N1}, T_{N2}, and T_3. (c) Detailed measurement of the dielectric constant ε (at the frequency $f = 903$ Hz) and the differential $d(\chi T)/dT$ (in arbitrary units) around T_{N1} and T_{N2} for $BaTmMnO_4$. Note that for $BaYbFeO_4$, weak anomalies in C_p/T, χ, and $d(\chi T)/dT$ around $T = 2.5$ K correspond to an antiferromagnetic transition in the Yb_2O_3 impurity.

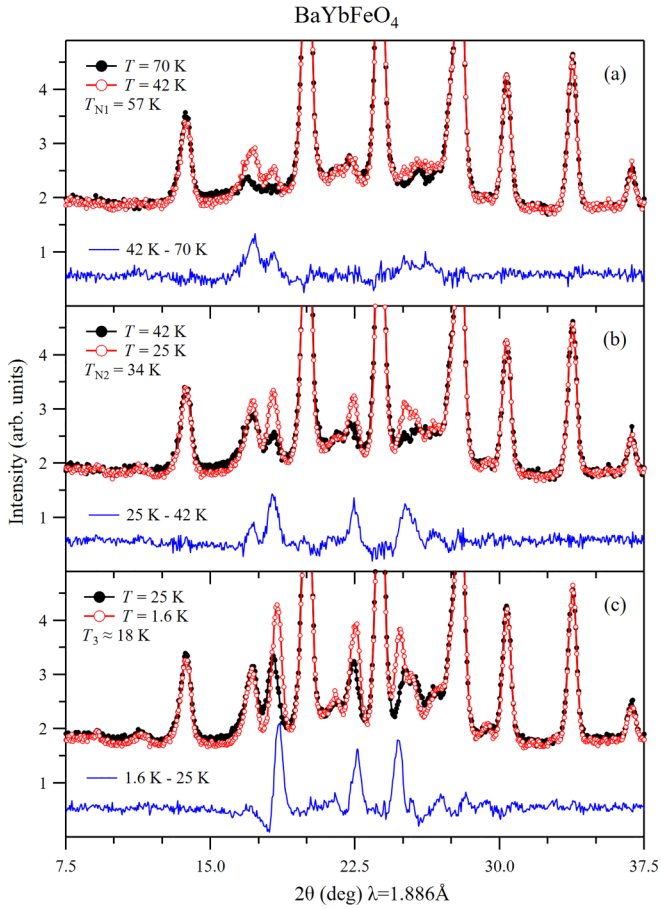

FIG. 4. Change of neutron-diffraction intensities of $BaYbFeO_4$ at the magnetic phase transitions at (a) $T_{N1} = 57$ K, (b) $T_{N2} = 34$ K, and (c) $T_3 \approx 18$ K. Difference patterns have been shifted by 0.6.

values is observed below $T_3 \approx 6$ K, but magnetic saturation of ordered Tm^{3+} moments is not yet reached at the lowest temperature $T = 1.6$ K of our experiment. The difference between T_{N1} and T_{N2} is large in $BaYbFeO_4$ (21 K) and small in $BaTmFeO_4$ (1.5 K). At T_{N2}, the dielectric constant ε exhibits a small peak in $BaTmFeO_4$ [Fig. 3(c)] and a local maximum in $BaYbFeO_4$ (see Fig. 4 of Ref. [8]) which demonstrates the coupling between magnetism and dielectric properties.

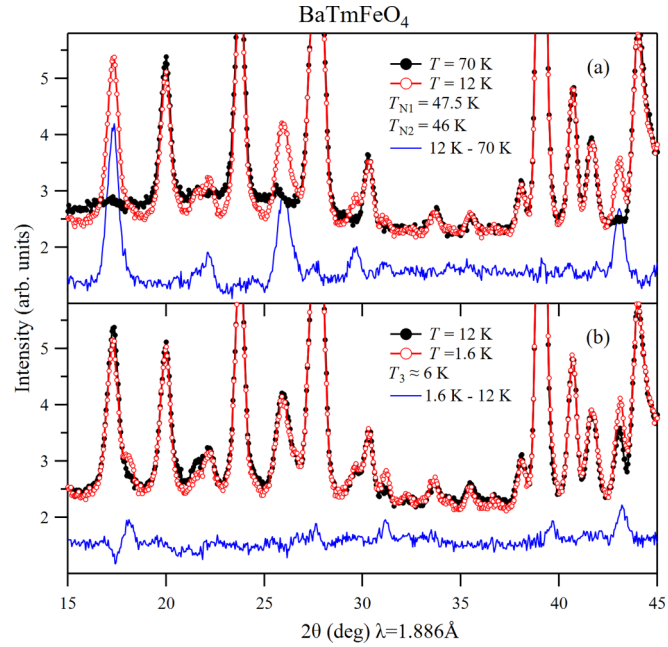

FIG. 5. Change of neutron-diffraction intensities of $BaTmFeO_4$ at the magnetic phase transitions at (a) $T_{N1} = 47.5$ K and $T_{N2} = 46$ K, and (b) $T_3 \approx 6$ K. Difference patterns have been shifted by 1.6.

Neutron-diffraction patterns measured above and below the phase transitions at T_{N1}, T_{N2}, and T_3 along with the difference intensity are shown in Fig. 4 (for $BaYbFeO_4$) and Fig. 5 (for $BaTmFeO_4$). For $BaTmFeO_4$, no neutron data have been measured between T_{N1} and T_{N2}. At all phase transitions, there is clear evidence for a change of the magnetic structures. For both compounds, $BaYbFeO_4$ and $BaTmFeO_4$, all observed magnetic Bragg peaks can be indexed with a temperature-dependent incommensurate magnetic propagation vector $\mathbf{k} = (0,\ 0,\ k_z)$. For the space group *Pnma*, site (4*c*) and this magnetic propagation vector, representation analysis for the possible magnetic structures gives the result summarized in Table III. There are four irreducible representations (irreps), *m*LD1, *m*LD2, *m*LD3, and *m*LD4, with different symmetry and the basis vectors are complex. The

TABLE III. Group-theory analysis for the magnetic structures of $BaTmFeO_4$ and $BaYbFeO_4$ calculated using the programs ISODISTORT [19] and BASIREPS [17]. The character set corresponds to the following four symmetry elements [17]: Symm(1): 1; Symm(2): 2 (0, 0, 1/2) 1/4, 0, *z*; Symm(3): *m x*, 1/4, *z*; Symm(4): *n* (0, 1/2, 1/2) 1/4, *y*, *z*. irrep denotes irreducible representation. The crystallographic space group is *Pnma* (No. 62). Magnetic propagation vector is $\mathbf{k} = (0,\ 0,\ k_z)$. $a = \exp(i\pi k_z)$. $a* = \exp(-i\pi k_z)$. All magnetic ions (Fe, Tm, Yb) are located on 4*c* sites. Components of the magnetic moments are expressed using $(u_1,\ v_1,\ w_1)$ and $(u_2,\ v_2,\ w_2)$ in orbits 1 and 2, respectively.

Character set	$(1,\ a,\ 1,\ a)$	$(1,\ a,\ -1,\ -a)$	$(1,\ -a,\ -1,\ a)$	$(1,\ -a,\ 1,\ -a)$
irrep (ISODISTORT)	*m*LD1	*m*LD2	*m*LD3	*m*LD4
irrep (BASIREPS)	IRrep(1)	IRrep(2)	IRrep(4)	IRrep(3)
Orbit 1:				
Fe_1, $R_1(x,\ 1/4,\ z)$	$(0,\ v_1,\ 0)$	$(u_1,\ 0,\ w_1)$	$(u_1,\ 0,\ w_1)$	$(0,\ v_1,\ 0)$
Fe_4, $R_4(-x+1/2,\ 3/4,\ z+1/2)$	$(0,\ -v_1,\ 0)\cdot a^*$	$(-u_1,\ 0,\ w_1)\cdot a^*$	$(u_1,\ 0,\ -w_1)\cdot a^*$	$(0,\ v_1,\ 0)\cdot a^*$
Orbit 2:				
Fe_3, R_3 $(-x,\ 3/4,\ -z)$	$(0,\ v_2,\ 0)$	$(u_2,\ 0,\ w_2)$	$(u_2,\ 0,\ w_2)$	$(0,\ v_2,\ 0)$
Fe_2, R_2 $(x+1/2,\ 1/4,\ -z+1/2)$	$(0,\ -v_2,\ 0)\cdot a^*$	$(-u_2,\ 0,\ w_2)\cdot a^*$	$(u_2,\ 0,\ -w_2)\cdot a^*$	$(0,\ v_2,\ 0)\cdot a^*$

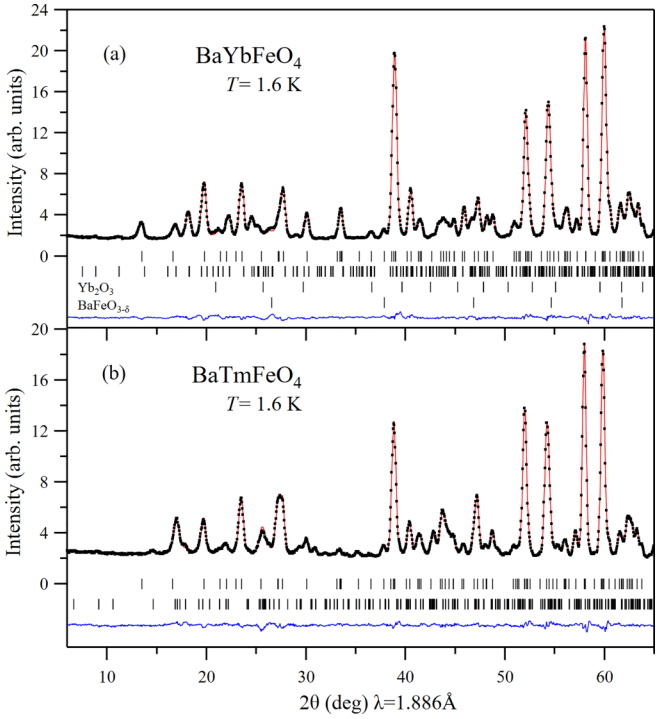

FIG. 6. Experimental (black dots), calculated (red line), and difference (blue line) neutron-diffraction patterns of $BaYbFeO_4$ (a) and $BaTmFeO_4$ (b) in the magnetically ordered state at $T = 1.6$ K. Tick marks indicate Bragg peak positions: the first row is for the nuclear peaks, and the second row is for the magnetic peaks. Impurity phases Yb_2O_3 and $BaFeO_{3-\delta}$ were included in the refinement of $BaYbFeO_4$.

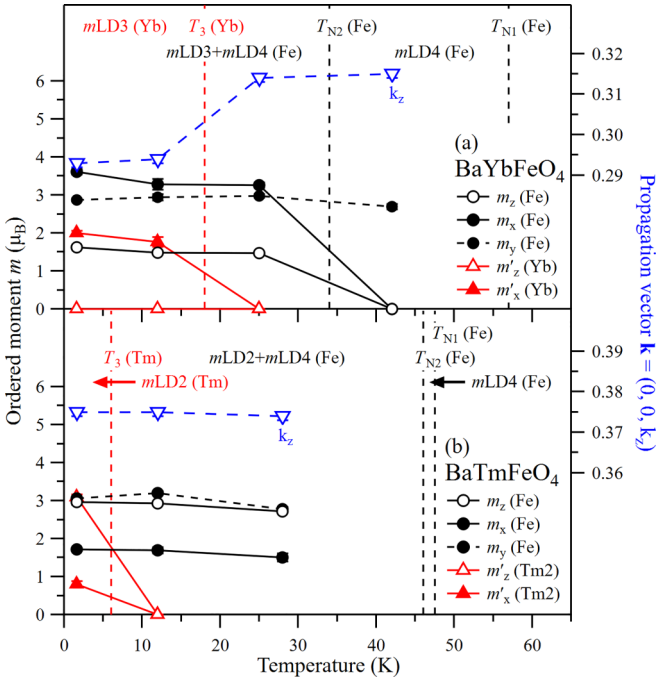

FIG. 7. Temperature dependence of the magnetic propagation vector $\mathbf{k} = (0,\ 0,\ k_z)$ and the components of the ordered magnetic moments $(m_x,\ m_y,\ m_z)$ and $(m'_x,\ 0,\ m'_z)$ for (a) $BaYbFeO_4$ and (b) $BaTmFeO_4$ determined by refinements of neutron-diffraction data. Vertical dashed lines indicate the magnetic phase transitions for $BaYbFeO_4$ ($T_{N1} = 57$ K, $T_{N2} = 34$ K, $T_3 \approx 18$ K) and for $BaTmFeO_4$ ($T_{N1} = 47.5$ K, $T_{N2} = 46$ K, $T_3 \approx 6$ K).

irreps *m*LD1 and *m*LD4 describe magnetic structures with ordered moments parallel to the *b* direction, whereas *m*LD2 and *m*LD3 correspond to structures with ordered moments inside the *ac* plane. Each irrep is split into two orbits (sets of magnetically nonequivalent sites) with the components of the magnetic moments expressed in Table III using $(u_1,\ v_1,\ w_1)$ and $(u_2,\ v_2,\ w_2)$, respectively. Among the 4 magnetic ions on site 4*c* (e.g., $Fe1_1$, $Fe1_2$, $Fe1_3$, $Fe1_4$), only the pairs separated by $\Delta z = 1/2$ are coupled by symmetry (e.g., $Fe1_1$ with $Fe1_4$, and $Fe1_3$ with $Fe1_2$). For magnetic ions that are not coupled by symmetry, it is necessary to determine the components of the ordered moments and in addition the magnetic phase δ. In summary, for the chains consisting of Fe^{3+} ions [see Fig. 2(b)], there is no symmetry coupling within one ring. But, within a certain irrep, the interchain coupling (components of ordered magnetic Fe moments and magnetic phase) is completely determined by symmetry. The same is valid for the two chains consisting of R^{3+} ions. To solve the magnetic structure, it is enough to determine the propagation vector k_z, the irrep, and the magnetic structure of one ring built by Fe^{3+} ions and one built by R^{3+} ions.

B. Magnetic structures of $BaYbFeO_4$

In the magnetically ordered state, magnetic and crystal structures of $BaYbFeO_4$ were simultaneously refined. The lower 2θ angle part of the refinements is shown in Fig. 6(a) ($T = 1.6$ K) and Fig. S2 [21] ($T = 25$ and 42 K). Magnetic Fe^{3+} moments are involved in the phase transitions at T_{N1} and T_{N2}, whereas an ordered Yb^{3+} moment appears below T_3. First, we checked for magnetic structures with a homogeneous distribution of the magnetic phase δ, where for each Fe^{3+} ion the phase is determined by the z component of its location ($\delta = z \cdot k_z$). For such refinements we obtained $R_{mag} = 8.95\%$ at $T = 25$ K. Next, we considered magnetic structures with an inhomogeneous distribution of the magnetic phase δ. The best agreement ($R_{mag} = 8.57\%$ at $T = 25$ K) was obtained for a magnetic structure, where the phase is constant inside the Fe ring and spin exchanges J_1 (between nearest neighbors) and J_2 (between next-nearest neighbors) are both strong and antiferromagnetic (see Fig. 2). The latter can be expected from the large bond angles $Fe1_1$–O1–$Fe2_2$ (168.5°) and $Fe1_1$–O5–$Fe2_4$ (172.9°). In such a magnetic structure, the intrachain couplings J_1 and J_2 are stronger than all other couplings and create collinear antiferromagnetic order of Fe^{3+} ions within each chain. Interchain spin exchanges through several paths determine the magnetic propagation vector (k_z) and the irrep. The results of the magnetic structure refinements for $BaYbFeO_4$ are given in Table IV and the temperature dependence of magnetic propagation vector and the components of the ordered Fe^{3+} and Yb^{3+} moments are plotted in Fig. 7(a).

At $T = 42$ K (between $T_{N1} = 57$ K and $T_{N2} = 34$ K), the propagation vector is $\mathbf{k} = (0,\ 0,\ k_z)$ with $k_z = 0.315(1)$ and ordered Fe moments of $m_y = 2.70(7)\ \mu_B$ are oriented perpendicular to $\mathbf{k}$. The magnetic structure is collinear and belongs to the irrep *m*LD4. It is a spin-density wave (SDW) with a correlation length of 70 ± 20 nm. The variation of the magnitude of the ordered Fe moments is large with

TABLE IV. Result of refinement of the magnetic structures of $BaYbFeO_4$ from powder neutron diffraction data. Positions of the magnetic ions Fe^{3+} and Yb^{3+} are labeled as shown in Fig. 2(b). Magnetic propagation vector $\mathbf{k} = (0,\ 0,\ k_z)$. Ordered magnetic Fe moments $(m_x,\ m_y,\ m_z)$ and Yb moments $(m'_x,\ 0,\ m'_z)$. The phase φ between the Fe(mLD3) and Fe(mLD4) components is 0.25 for model No. 1 and 0 for model No. 2. Maximum and minimum ordered Fe moments $(M_{\max},\ M_{\min})$ and Yb moments $(M'_{\max},\ M'_{\min})$. Magnetic phase $\delta = 0, \pm\alpha$; where $\alpha = k_z/2$.

Ion	$T = 42$ K	$T = 25, 12, 1.6$ K	Ion	$T = 12, 1.6$ K
$Fe1_1$	$(0,\ m_y,\ 0), 0$	$(m_x,\ m_y,\ -m_z), 0$	$Yb1_1$	$(-m'_x,\ 0,\ -m'_z),\ -\alpha$
$Fe1_2$	$(0,\ m_y,\ 0), \alpha$	$(m_x,\ m_y,\ m_z), \alpha$	$Yb1_2$	$(-m'_x,\ 0,\ m'_z), 0$
$Fe1_3$	$(0,\ m_y,\ 0), 0$	$(m_x,\ m_y,\ -m_z), 0$	$Yb1_3$	$(-m'_x,\ 0,\ -m'_z),\ -\alpha$
$Fe1_4$	$(0,\ m_y,\ 0), \alpha$	$(m_x,\ m_y,\ m_z), \alpha$	$Yb1_4$	$(-m'_x,\ 0,\ m'_z), 0$
$Fe2_1$	$(0,\ -m_y,\ 0), \alpha$	$(-m_x,\ -m_y,\ -m_z), \alpha$	$Yb2_1$	$(m'_x,\ 0,\ -m'_z), 0$
$Fe2_2$	$(0,\ -m_y,\ 0), 0$	$(-m_x, -m_y, m_z), 0$	$Yb2_2$	$(m'_x,\ 0,\ m'_z), -\alpha$
$Fe2_3$	$(0,\ -m_y,\ 0), \alpha$	$(-m_x,\ -m_y,\ -m_z), \alpha$	$Yb2_3$	$(m'_x,\ 0,\ -m'_z), 0$
$Fe2_4$	$(0,\ -m_y,\ 0), 0$	$(-m_x, -m_y, m_z), 0$	$Yb2_4$	$(m'_x,\ 0,\ m'_z), -\alpha$
$T = 42$ K:	$k_z = 0.315(1)$; $\chi^2 = 2.46$; $R_{wp} = 2.81\%$; $R_{exp} = 1.79\%$; $R_{Bragg} = 1.38\%$; $R_{mag} = 7.31\%$ Fe (mLD4): $m_y = 2.70(7)\ \mu_B$; $M_{\max}(Fe) = 2.70(7)\ \mu_B$; $M_{\min}(Fe) = 0\ \mu_B$			
$T = 25$ K:	$k_z = 0.314(1)$; $\chi^2 = 4.21$; $R_{wp} = 2.81\%$; $R_{exp} = 1.37\%$; $R_{Bragg} = 1.34\%$; $R_{mag} = 8.57\%$ Fe (mLD3): $m_x = 3.26(7)\ \mu_B$; $m_z = 1.47(3)\ \mu_B$; Fe (mLD4): $m_y = 2.98(5)\ \mu_B$ Model No. 1: $M_{\max,\ No.\ 1}(Fe) = 3.57(8)\ \mu_B$; $M_{\min,\ No.\ 1}(Fe) = 2.98(5)\ \mu_B$ Model No. 2: $M_{\max,\ No.\ 2}(Fe) = 4.65(7)\ \mu_B$; $M_{\min,\ No.\ 2}(Fe) = 0\ \mu_B$			
$T = 12$ K:	$k_z = 0.294(1)$; $\chi^2 = 1.34$; $R_{wp} = 5.08\%$; $R_{exp} = 4.39\%$; $R_{Bragg} = 1.76\%$; $R_{mag} = 6.65\%$ Fe (mLD3): $m_x = 3.28(14)\ \mu_B$; $m_z = 1.48(6)\ \mu_B$; Fe (mLD4): $m_y = 2.94(8)\ \mu_B$ Yb (mLD3): $m'_x = 1.77(13)\ \mu_B$; $m'_z \approx 0\ \mu_B$; $M'_{\max}(Yb) = 1.77(13)\ \mu_B$; $M'_{\min}(Yb) = 0\ \mu_B$ Model No. 1: $M_{\max,\ No.\ 1}(Fe) = 3.60(15)\ \mu_B$; $M_{\min,\ No.\ 1}(Fe) = 2.94(8)\ \mu_B$ Model No. 2: $M_{\max,\ No.\ 2}(Fe) = 4.65(13)\ \mu_B$; $M_{\min,\ No.\ 2}(Fe) = 0\ \mu_B$			
$T = 1.6$ K:	$k_z = 0.293(2)$; $\chi^2 = 3.99$; $R_{wp} = 2.77\%$; $R_{exp} = 1.39\%$; $R_{Bragg} = 1.24\%$; $R_{mag} = 6.23\%$ Fe (mLD3): $m_x = 3.61(7)\ \mu_B$; $m_z = 1.62(3)\ \mu_B$; Fe (mLD4): $m_y = 2.87(4)\ \mu_B$ Yb (mLD3): $m'_x = 2.00(7)\ \mu_B$; $m'_z \approx 0$; $M'_{\max}(Yb) = 2.00(7)\ \mu_B$; $M'_{\min}(Yb) = 0\ \mu_B$ Model No. 1: $M_{\max,\ No.\ 1}(Fe) = 3.96(8)\ \mu_B$; $M_{\min,\ No.\ 1}(Fe) = 2.87(4)\ \mu_B$ Model No. 2: $M_{\max,\ No.\ 2}(Fe) = 4.89(7)\ \mu_B$; $M_{\min,\ No.\ 2}(Fe) = 0\ \mu_B$			
$Fe1_1$ (0.469, 0.25, 0.717); $Fe1_2$ (0.969, 0.25, 0.783); $Fe1_3$ (0.531, 0.75, 0.283); $Fe1_4$ (1.031, 0.75, 1.217) $Fe2_1$ (1.191, 0.25, 1.023); $Fe2_2$ (0.691, 0.25, 0.477); $Fe2_3$ (0.809, 0.75, 0.977); $Fe2_4$ (0.309, 0.75, 0.523)				
$Yb1_1$ (0.415, 0.25, 0.014); $Yb1_2$ (0.915, 0.25, 0.486); $Yb1_3$ (0.585, 0.75, −0.014); $Yb1_4$ (1.085, 0.75, 0.514) $Yb2_1$ (1.143, 0.25, 0.310); $Yb2_2$ (0.643, 0.25, 0.190); $Yb2_3$ (0.857, 0.75, 0.690); $Yb2_4$ (0.357, 0.75, −0.190)				

$M_{\max}(Fe) = 2.70(7)\ \mu_B$ and $M_{\min}(Fe) = 0\ \mu_B$. The agreement of this structure with the experimental data is good. Allowing different values of the ordered moments at Fe1 (square pyramids) and Fe2 (octahedral) does not further improve the quality of the refinement.

When cooling through T_{N2} to $T = 25$ K, the propagation vector $k_z = 0.314(1)$ remains almost unchanged and the mLD4 component of the ordered Fe moments remains stable $[m_y = 2.98(5)\ \mu_B]$. Below T_{N2}, an additional component belonging to the irrep mLD3 appears inside the ac plane $[m_x = 3.26(7)\ \mu_B,\ m_z = 1.47(3)\ \mu_B]$ and the correlation length increased to 190 ± 25 nm at $T = 25$ K. The magnetic structure is noncollinear and corresponds to a superposition of the irreps mLD3 and mLD4. The magnetic structure has a lower symmetry than a cycloid ($m_x = 0$) or a helix ($m_z = 0$, $m_x = m_y$). It is a cycloidal spiral magnetic structure [23,24] that can be viewed as a sum of a cycloid and a helix structure due to the presence of modulated components both parallel and perpendicular to the propagation vector $\mathbf{k}$. This structure of ordered Fe moments remains stable down to the lowest measured temperature $T = 1.6$ K. The phase υ between the Fe(mLD3) component $(m_x,\ m_z)$ and the Fe(mLD4) component (m_y) cannot be determined in our powder neutron diffraction experiment. The calculated neutron intensities are the same for $\upsilon = 0.25$ (model No. 1) and $\upsilon = 0$ (model No. 2). Both models equally well agree with the experimental data.

For model No. 1 ($\upsilon = 0.25$), the mLD4 component describes the imaginary part and the mLD3 component the real part of a magnetic structure, where the ordered Fe moments rotate on an ellipsoid inside the plane defined by the $(m_x + m_z)$ and the m_y directions [Fig. 8(c)]. The magnetic propagation vector $\mathbf{k}$ (c direction) lies outside this plane at an angle $\varphi(Fe)$ of $66^\circ \pm 1^\circ$ [Fig. 8(b)]. The variation of the magnitude of the ordered Fe moments becomes small $[M_{\max,\ No.\ 1}(Fe) = 3.96(8)\ \mu_B,\ M_{\min,\ No.\ 1}(Fe) = 2.87(4)\ \mu_B]$ and the values are reduced below the full Fe^{3+} moment of $5.0\ \mu_B$. For model No. 2 ($\upsilon = 0$), ordered Fe moments point along the $m_x + m_y + m_z$ direction with a large variation of the amplitudes $[M_{\max,\ No.\ 2}(Fe) = 4.89(7)\mu_B,\ M_{\min,\ No.\ 2}(Fe) = 0\ \mu_B]$ and the maximum value close to the full Fe^{3+} moment. The magnetic structures of $BaYbFeO_4$ at $T = 1.6$ K are illustrated in Fig. 9 for model No. 1 and Fig. S3 [21] for model No. 2. Inside the ac

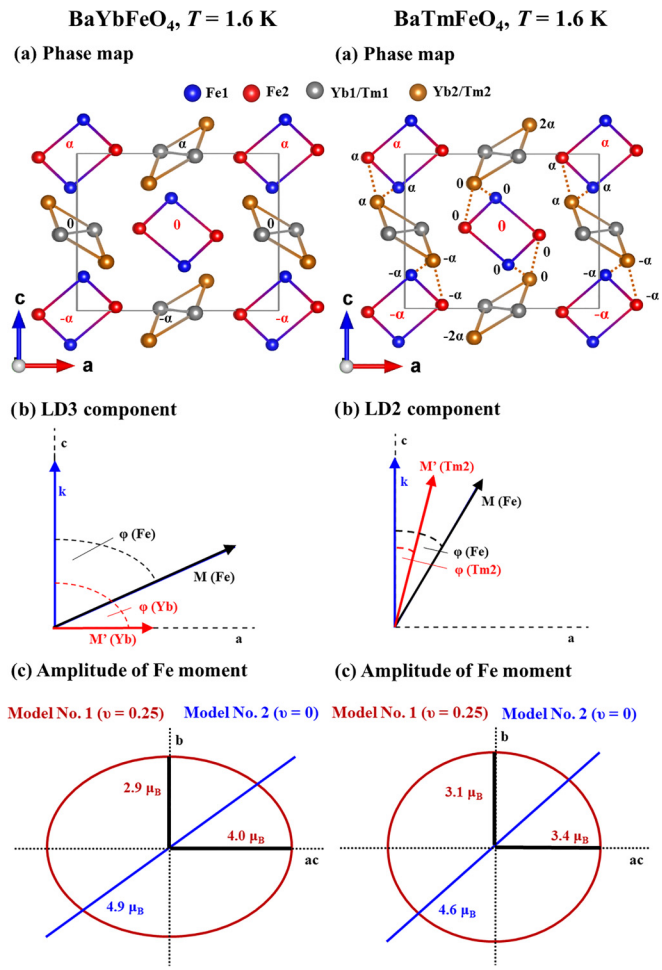

FIG. 8. Magnetic structures of $BaYbFeO_4$ and $BaTmFeO_4$ at $T = 1.6$ K. (a) Phase maps. (b) mLD3/mLD2 components of the ordered moments. $\varphi(\mathrm{Fe}) = 66(1)^\circ$ and $\varphi(\mathrm{Yb}) \approx 90^\circ$ for $BaYbFeO_4$. $\varphi(\mathrm{Fe}) = 30(1)^\circ$ and $\varphi(\mathrm{Tm2}) = 15(2)^\circ$ for $BaTmFeO_4$. (c) Variation of the amplitude of the ordered Fe moment for models No. 1 and No. 2. Direction inside the ac plane corresponds to the direction of M(Fe) shown in (b). Drawings were partly made using the program VESTA [22].

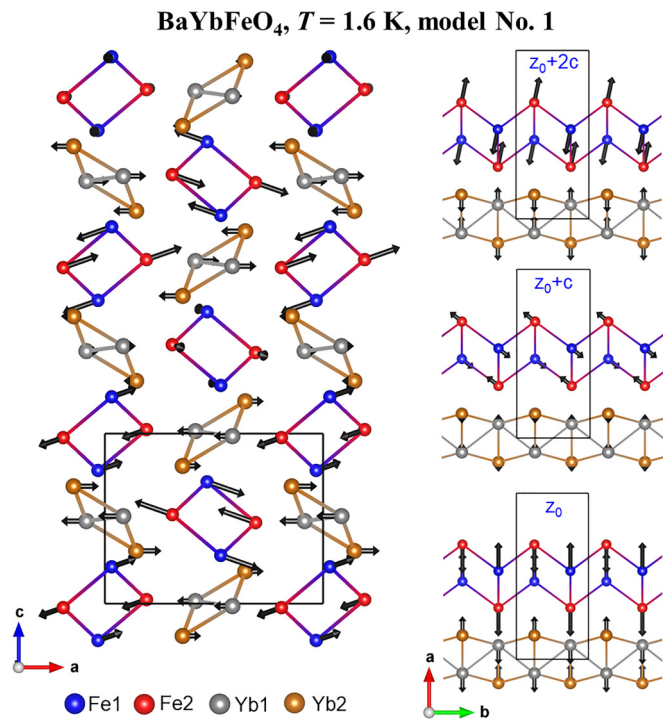

FIG. 9. Illustration of the noncollinear incommensurate magnetic structure of $BaYbFeO_4$ at $T = 1.6$ K for model No. 1 shown as a projection onto the ac- and ab planes. Latter is shown at z_0, $z_0 + c$, and $z_0 + 2c$. Drawings were made using the program VESTA [22].

plane, the components of the ordered moments are the same for both models.

Long-range magnetic order of Yb^{3+} ions, belonging to the irrep mLD3, appears below $T_3 \approx 18$ K. Ordered Yb^{3+} moments [$m'_x = 1.77(13)$ μ_B at 12 K and $m'_x = 2.00(6)$ μ_B at 1.6 K] align perpendicular to **k**. Within the accuracy of our experiment, a possible component parallel to **k** (m'_z) is zero or close to zero. The magnetic entropy released by ordering of Yb^{3+} moments can be seen by a C_p/T anomaly with a peak around 11 K [Fig. 3(a)]. At $T = 12$ K, ordered Yb^{3+} moments already reach about 90% of the saturation value. The appearance of long-range magnetic Yb^{3+} order affects the interchain couplings and leads to a decrease of about 4% of the magnetic propagation vector from $k_z = 0.314(1)$ at $T = 25$ K to $k_z = 0.294(1)$ at $T = 12$ K. k_z is almost temperature independent between 42 and 25 K and again between 12 and 1.6 K. The correlation length of the magnetic structure increases from about 190 nm at $T = 25$ K to around 500 nm at 12 and 1.6 K. Magnetic order of Yb^{3+} ions is stabilized by $4f$ electron-exchange interactions. Similar to the Fe^{3+} ions, each ring and chain formed by Yb^{3+} ions has a constant magnetic phase δ and antiferromagnetic coupling between Yb nearest neighbors and next-nearest neighbors. As displayed in the phase map [Fig. 8(a)], perpendicular to the magnetic propagation vector $\mathbf{k} = (0,\ 0,\ k_z)$, there are rows of chains consisting of Fe^{3+} and Yb^{3+} ions with a constant magnetic phase δ. Along **k**, δ changes with discrete values of $\alpha = k_z/2$.

C. Magnetic structures of $BaTmFeO_4$

In the magnetically ordered state, magnetic and crystal structures of $BaTmFeO_4$ were simultaneously refined. The lower 2θ angle part of the refinements is shown in Fig. 6(b) ($T = 1.6$ K) and Fig. S4 [21] ($T = 12$ and 28 K). The results of the magnetic structure refinements are given in Table V and the temperature dependence of magnetic propagation vector and the components of the ordered Fe^{3+} and Tm^{3+} moments are plotted in Fig. 7(b).

Below $T = 28$ K, the magnetic structure of $BaTmFeO_4$ has an almost temperature-independent propagation vector [$k_z = 0.375(1)$ at $T = 1.6$ K] with a value close to 3/8. Also, the correlation length of 230(50) nm remains essentially temperature independent. Fe^{3+} moments are ordered with a superposition of the irreps mLD2 and mLD4 and only a weak temperature dependence. At $T = 1.6$ K, ordered Fe^{3+} moments are inside the ac plane [$m_x = 1.72(3)$ μ_B, $m_z = 2.96(6)$ μ_B] for the mLD2 component and along the

TABLE V. Result of refinement of the magnetic structures of $BaTmFeO_4$ from powder neutron diffraction data. Positions of the magnetic ions Fe^{3+} and Tm^{3+} are labeled as shown in Fig. 2(b). Magnetic propagation vector $\mathbf{k} = (0,\ 0,\ k_z)$. Ordered magnetic Fe moments $(m_x,\ m_y,\ m_z)$ and Tm2 moments $(m'_x,\ 0,\ m'_z)$. The phase φ between the Fe(mLD2) and Fe(mLD4) components is 0.25 for model No. 1 and 0 for model No. 2. Maximum and minimum ordered Fe moments $(M_{\max},\ M_{\min})$ and Tm2 moments $(M'_{\max},\ M'_{\min})$. Magnetic phase $\delta = 0, \pm\alpha, -2\alpha$; where $\alpha = k_z/2$.

Ion	$T = 28, 12, 1.6$ K	Ion	$T = 1.6$ K
$Fe1_1$	$(m_x,\ m_y,\ m_z), 0$	$Tm1_1$	
$Fe1_2$	$(-m_x,\ m_y,\ m_z), \alpha$	$Tm1_2$	
$Fe1_3$	$(m_x,\ m_y,\ m_z), 0$	$Tm1_3$	
$Fe1_4$	$(-m_x,\ m_y,\ m_z), \alpha$	$Tm1_4$	
$Fe2_1$	$(m_x,\ -m_y,\ -m_z), \alpha$	$Tm2_1$	$(-m'_x,\ 0,\ m'_z), -\alpha$
$Fe2_2$	$(-m_x,\ -m_y,\ -m_z), 0$	$Tm2_2$	$(m'_x,\ 0,\ m'_z), 0$
$Fe2_3$	$(m_x,\ -m_y,\ -m_z), \alpha$	$Tm2_3$	$(-m'_x,\ 0,\ m'_z), \alpha$
$Fe2_4$	$(-m_x,\ -m_y,\ -m_z), 0$	$Tm2_4$	$(m'_x,\ 0,\ m'_z), -2\alpha$
$T = 28$ K:	$k_z = 0.374(1)$; $\chi^2 = 2.02$; $R_{wp} = 2.92\%$; $R_{exp} = 2.06\%$; $R_{Bragg} = 1.51\%$; $R_{mag} = 7.80\%$ Fe (mLD2): $m_x = 1.51(10)\ \mu_B$; $m_z = 2.72(10)\ \mu_B$; Fe (mLD4): $m_y = 2.78(6)\ \mu_B$ Model No. 1: $M_{\max,\ No.\ 1}(Fe) = 3.11(9)\ \mu_B$; $M_{\min,\ No.\ 1}(Fe) = 2.78(6)\ \mu_B$ Model No. 2: $M_{\max,\ No.\ 2}(Fe) = 4.17(6)\ \mu_B$; $M_{\min,\ No.\ 2}(Fe) = 0\ \mu_B$		
$T = 12$ K:	$k_z = 0.375(1)$; $\chi^2 = 3.24$; $R_{wp} = 2.49\%$; $R_{exp} = 1.39\%$; $R_{Bragg} = 1.41\%$; $R_{mag} = 6.73\%$ Fe (mLD2): $m_x = 1.70(8)\ \mu_B$; $m_z = 2.93(8)\ \mu_B$; Fe (mLD4): $m_y = 3.20(5)\ \mu_B$ Model No. 1: $M_{\max,\ No.\ 1}(Fe) = 3.38(7)\ \mu_B$; $M_{\min,\ No.\ 1}(Fe) = 3.20(5)\ \mu_B$ Model No. 2: $M_{\max,\ No.\ 2}(Fe) = 4.65(5)\ \mu_B$; $M_{\min,\ No.\ 2}(Fe) = 0\ \mu_B$		
$T = 1.6$ K:	$k_z = 0.375(1)$; $\chi^2 = 3.27$; $R_{wp} = 2.63\%$; $R_{exp} = 1.45\%$; $R_{Bragg} = 1.43\%$; $R_{mag} = 8.15\%$ Fe (mLD2): $m_x = 1.72(3)\ \mu_B$; $m_z = 2.96(6)\ \mu_B$; Fe (mLD4): $m_y = 3.06(4)\ \mu_B$ Tm2 (mLD2): $m'_x = 0.80(8)\ \mu_B$; $m'_z = 3.10(7)\ \mu_B$; $M'_{\max}(Tm2) = 3.20(7)\ \mu_B$; $M'_{\min}(Tm2) = 0\ \mu_B$ Model No. 1: $M_{\max,\ No.\ 1}(Fe) = 3.42(7)\ \mu_B$; $M_{\min,\ No.\ 1}(Fe) = 3.06(4)\ \mu_B$ Model No. 2: $M_{\max,\ No.\ 2}(Fe) = 4.59(5)\ \mu_B$; $M_{\min,No.\ 2}(Fe) = 0\ \mu_B$		
$Fe1_1$ (0.469, 0.25, 0.717); $Fe1_2$ (0.969, 0.25, 0.783); $Fe1_3$ (0.531, 0.75, 0.283); $Fe1_4$ (1.031, 0.75, 1.217) $Fe2_1$ (1.190, 0.25, 1.024); $Fe2_2$ (0.690, 0.25, 0.476); $Fe2_3$ (0.810, 0.75, 0.976); $Fe2_4$ (0.310, 0.75, 0.524) $Tm1_1$ (0.415, 0.25, 0.015); $Tm1_2$ (0.915, 0.25, 0.485); $Tm1_3$ (0.585, 0.75, −0.015); $Tm1_4$ (1.085, 0.75, 0.515) $Tm2_1$ (1.143, 0.25, 0.311); $Tm2_2$ (0.643, 0.25, 0.189); $Tm2_3$ (0.857, 0.75, 0.689); $Tm2_4$ (0.357, 0.75, −0.189)			

b direction $[m_y = 3.06(4)\ \mu_B]$ for the mLD4 component. Detailed measurement of $d(\chi T)/dT$ shown in Fig. 3(c) suggests successive magnetic order of the mLD4 component at $T_{N1} = 47.5$ K and the mLD2 component at $T_{N2} = 46$ K. The specific-heat data shown in Fig. 3(b) indicate that both phase transitions at T_{N1} and T_{N2} are of second order. The irreps mLD4 and mLD2 have two different order parameters. Therefore, according to Landau theory [25], magnetic ordering occurs in two successive second-order phase transitions at T_{N1} and T_{N2}, which supports the interpretation of our more-detailed $d(\chi T)/dT$ data shown in Fig. 3(c). No neutron data have been collected between T_{N1} and T_{N2}.

We present the results for $BaTmFeO_4$ in a similar way as in Sec. III B for $BaYbFeO_4$. Below $T = 28$ K, the magnetic structure of Fe^{3+} moments in $BaTmFeO_4$ is a cycloidal spiral magnetic structure that can be viewed as a sum of a cycloid and a helix structure due to the presence of modulated components both parallel and perpendicular to the propagation vector $\mathbf{k}$. For model No. 1 ($\upsilon = 0.25$) at $T = 1.6$ K, the magnetic propagation vector $\mathbf{k}$ (c direction) lies outside the plane of ordered Fe moments at an angle φ(Fe) of $30^\circ \pm 1^\circ$ [Fig. 8(b)] and the variation of the amplitude of ordered Fe^{3+} moments between $3.06(4)\mu_B$ and $3.42(7)\mu_B$ is small [Fig. 8(c), Table V]. For model No. 2 ($\upsilon = 0$) at $T = 1.6$ K, the ordered Fe^{3+} moments vary on a straight line $(m_x + m_y + m_z)$ and reach a maximum value of $4.59(5)\mu_B$ [Fig. 8(c), Table V]. The magnetic structures of $BaTmFeO_4$ at $T = 1.6$ K are illustrated in Fig. 10 for model No. 1 and Fig. S5 [21] for model No. 2.

Below $T_3 \approx 6$ K, the specific heat C_p/T of $BaTmFeO_4$ shows a strong increase towards the lowest measured temperature $T = 1.6$ K [Fig. 3(b)]. The changes of the neutron-diffraction intensities measured at $T = 12$ and 1.6 K [Fig. 5(b)] cannot be explained by magnetic ordering of Fe^{3+} moments alone. The refinement of the neutron pattern measured at $T = 1.6$ K revealed a nonzero ordered Tm2 moment and a disordered Tm1 moment. Including an ordered Tm2 moment into the refinement at $T = 12$ K gives a value close to zero. The ordered Tm2 moments appear between $T = 12$ and 1.6 K at $T_3 \approx 6$ K. As listed in Table II and indicated by yellow dashed lines in Fig. 8(a), each Tm2 ion has one Fe2 neighbor (at 2.987 Å) and two Fe1 neighbors (at 3.326 Å) with the same magnetic phase δ. Based on $3d-4f$ electron spin-exchange interactions, these Fe ions induce an ordered moment at the Tm2 neighbor with the same magnetic phase δ. As a result, inside each ring, the two Tm2 ions are ordered with a magnetic phase difference of $\Delta\delta = k_z(= 2\alpha)$, and therefore have a different amplitude (Fig. 10). Due to frustration of magnetic exchange interactions the Tm1 ions remain disordered. The phase map is shown in Fig. 8(a). At the

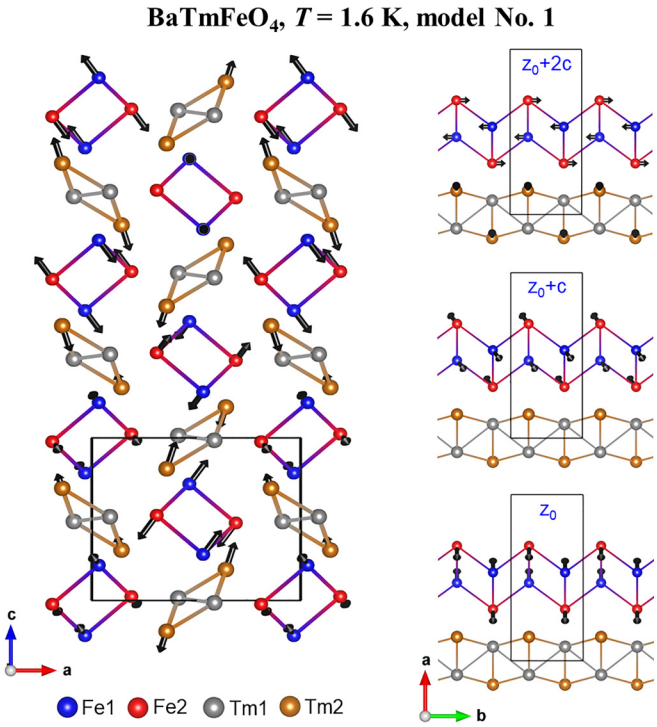

FIG. 10. Illustration of the noncollinear incommensurate magnetic structure of $BaTmFeO_4$ at $T = 1.6$ K for model No. 1 shown as a projection onto the *ac*- and *ab* planes. Latter is shown at z_0, $z_0 + c$, and $z_0 + 2c$. Drawings were made using the program VESTA [22].

lowest measured temperature $T = 1.6$ K, magnetic saturation of the ordered Tm moments is probably not yet reached. As shown in Fig. 8(b), Tm2 moments are ordered inside the *ac* plane within the irrep *m*LD2 at an angle $\varphi(\text{Tm2}) = 15(2)^\circ$ with the magnetic propagation vector **k** (*c* direction). Down to $T = 1.6$ K, spin exchanges between $4f$ electrons cannot produce a long-range magnetic structure of Tm^{3+} ions as has been observed for Yb^{3+} in $BaYbFeO_4$. In $BaTmFeO_4$, the appearance of induced magnetic order at $Tm2^{3+}$ by $3d-4f$ electron spin exchanges does not affect the interchain coupling of Fe^{3+} ions and the magnetic propagation vector k_z remains almost temperature independent at a value close to 3/8.

D. Comparison of the magnetic structures

The magnetic structures of $BaYbFeO_4$ (this work), $BaTmFeO_4$ (this work), and $BaYFeO_4$ [11] are compared in Table VI. These materials belong to a group of isostructural ferrite compounds, where the incommensurate magnetic propagation vector $\mathbf{k} = (0,\ 0,\ k_z)$ is stable. As a common feature, long-range magnetic ordering of Fe1 and Fe2 occurs in two successive magnetic phase transitions with a collinear spin-density wave structure below T_{N1} and a noncollinear antiferromagnetic structure below T_{N2}. For $BaTmFeO_4$, Mössbauer experiments [9] suggested the presence of SDW structure between T_{N1} and T_{N2}. Two different irreps order at T_{N1} and T_{N2}. The magnetic structures belong to only one irrep below T_{N1} and to a coexistence of two irreps below T_{N2}.

TABLE VI. Comparison of the magnetic structures of $BaYbFeO_4$, $BaTmFeO_4$, and $BaYFeO_4$. Magnetic ordering temperatures (T_{N1}, T_{N2}, T_3). Magnetic propagation vector $\mathbf{k} = (0,\ 0,\ k_z)$. Maximum ($M_{max}$, M'_{max}) and minimum (M_{min}) ordered Fe moment (M) and Yb/Tm2 moment (M') for model No. 1. φ(Fe), φ(Yb/Tm2); angle between **k** and **M** (Fe), **M**′ (Yb/Tm2) shown in Fig. 8(b). irrep: irreducible representation. *: no neutron data available.

	$BaYbFeO_4$ (This work)	$BaTmFeO_4$ (This work)	$BaYFeO_4$ [11]
T_{N1}, T_{N2}, T_3 (K)	57, 36, ≈ 18	47.5, 46, ≈ 6	48, 36, –
$T_{N2} < T < T_{N1}$ (Fe): irrep	*m*LD4	*m*LD4	*m*LD4
Structure type	SDW	SDW	SDW
$\mathbf{k} = (0,\ 0,\ k_z)$; T	$k_z = 0.315(1)$; 42 K	*	$k_z = 0.333$; 38 K
$M(\mu_B)$; T	2.70(7); 42 K	*	2.2(2); 3.0(2); 38 K
$T < T_{N2}$ (Fe): irrep	*m*LD4 + *m*LD3	*m*LD4 + *m*LD2	*m*LD4 + *m*LD2
Structure type	Cycloidal spiral	Cycloidal spiral	Cycloid
$\mathbf{k} = (0,\ 0,\ k_z)$; T	$k_z = 0.314(1)$; 25 K	$k_z = 0.374(1)$; 28 K	$k_z = 0.358(2)$; 6 K
	$k_z = 0.294(1)$; 12 K	$k_z = 0.375(1)$; 12 K	
	$k_z = 0.293(2)$; 1.6 K	$k_z = 0.375(1)$; 1.6 K	
$M_{max}(\mu_B)$; $M_{min}(\mu_B)$; T	3.57(8); 2.98(5); 25 K	3.11(9); 2.78(6); 28 K	3.0(1); 2.8(1); 6 K
	3.60(15); 2.94(8); 12 K	3.38(7); 3.20(5); 12 K	
	3.96(8); 2.87(4); 1.6 K	3.42(7); 3.06(4); 1.6 K	
Angle: φ(Fe); T	66(1)°; 1.6 K	30(1)°; 1.6 K	0°; 6 K
$T < T_3$ (Yb/Tm2): irrep	*m*LD3	*m*LD2	
$M'_{max}(\mu_B)$; T	1.77(13); 12 K	3.20(7); 1.6 K	
	2.00(7); 1.6 K		
Angle: φ(Yb/Tm2); T	∼90°; 1.6 K	15(2)°; 1.6 K	

For $BaYFeO_4$, the relative strengths of magnetic exchange interactions along various possible pathways were studied by extended Hückel spin-dimer analysis [10]. The theoretical work suggested that only interactions between square pyramidal (Fe1) and octahedral (Fe2) centers are significant. Among them, the antiferromagnetic intrachain interactions J_1 and J_2 [indicated in Fig. 2(b)] are much stronger than the interchain Fe-Fe interactions. According to the results of our work, also $BaYbFeO_4$ and $BaTmFeO_4$ show such a behavior. Inside each chain, strong antiferromagnetic Fe-Fe spin-exchange coupling generates a collinear antiferromagnetic structure with a constant magnetic phase. Inside the unit cell, the two Fe chains have different chirality [Fig. 2(b)] and a noncollinear coupling. Interchain Fe-Fe coupling is weaker and determines the value of the propagation vector k_z and the choice of the irrep. The different behavior between the three compounds reflects the different magnetic anisotropy and size of the magnetic R^{3+} ions. Due to the mixing of two irreps below T_{N2}, the crystal and magnetic symmetry is lowered down to monoclinic, $P2_1$ (for mLD4 + mLD3 in $BaYbFeO_4$) and Pb (for mLD4 + mLD2 in $BaYFeO_4$ and $BaTmFeO_4$) [19].

Motivated by the magnetic structure determination of $BaYFeO_4$ [11], a theoretical study based on spin-polarized density-functional theory calculations [13] suggested that the SDW structure ($T_{N2} < T < T_{N1}$) arises from a superposition of two equally populated magnetic states of opposite chirality. As temperature decreases ($T < T_{N2}$), the crystal lattice relaxes, so the two states become nondegenerate to give rise to a noncollinear magnetic structure such as a cycloidal structure in $BaYFeO_4$. For $BaYbFeO_4$ and $BaTmFeO_4$, the symmetry of the magnetic structure below T_{N2} is even lower than cycloidal. It is a cycloidal spiral magnetic structure that can be viewed as a sum of a cycloid and a helix structure. Ordered Fe moments rotate on an ellipsoid inside a plane (model No. 1) that forms an angle φ(Fe) with the propagation vector $\mathbf{k}$ of $\sim 66^\circ$ for $BaYbFeO_4$ and $\sim 30^\circ$ for $BaTmFeO_4$ [Fig. 8(b)]. $BaYFeO_4$ is a spin-driven multiferroic system [12]. As described by the spin-current model [26], magnetodielectric coupling induces an electric polarization below T_{N2} by the noncollinear cycloidal spin structure with $\varphi(\text{Fe}) = 0^\circ$. The magnetic structure of $BaTmFeO_4$ is closer to a cycloid, and a small sharp peak in the dielectric constant observed at T_{N2} [Fig. 3(c)] demonstrates the coupling of magnetic and dielectric properties. The magnetic structure of $BaYbFeO_4$ is closer to a helix [$\varphi(\text{Fe}) = 90^\circ$] and the dielectric constant shows a broad peak around T_{N2} (Fig. 4 of Ref. [8]).

Magnetic ordering of the rare-earth ions at T_3 occurs within the irreducible representation that appeared at T_{N2} (mLD3 in $BaYbFeO_4$ and mLD2 in $BaTmFeO_4$) within the ac plane. For BaYbFeO4 with the smallest R^{3+} ionic radius, at lower temperature, long-range magnetic ordering of Yb^{3+} ions is stabilized by $4f-4f$ electron spin-exchange coupling. Each Yb chain orders with a collinear antiferromagnetic structure and a constant magnetic phase. In contrast, for BaTmFeO4 with the second-smallest R^{3+} ionic radius, magnetic order of Tm^{3+} ions is induced by $3d-4f$ electron spin-exchange coupling. Inside each Tm ring, the two Tm2 ions order with a magnetic phase difference of $\Delta\delta = k_z$, and the two Tm1 ions remain disordered due to frustration of magnetic exchange interactions. A partially disorder state has been observed in several frustrated antiferromagnets [27–30].

IV. CONCLUSION

Based on detailed macroscopic measurements (specific heat and magnetic susceptibility) we showed that the ferrite materials $BaYbFeO_4$ and $BaTmFeO_4$ undergo three successive magnetic phase transitions, similar to all other members of the BaRFeO$_4$ series with magnetic rare-earth cations. We employed neutron diffraction to extend the determination of the magnetic structures from $BaYFeO_4$ ($T_{N1} = 48$ K, $T_{N2} = 36$ K) with purely $3d$ electron magnetism [11] to $BaYbFeO_4$ ($T_{N1} = 57$ K, $T_{N2} = 34$ K, $T_3 \approx 18$ K) and $BaTmFeO_4$ ($T_{N1} = 47.5$ K, $T_{N2} = 46$ K, $T_3 \approx 6$ K) with coexisting $3d$ and $4f$ electron magnetism. These compounds belong to a group of isostructural ferrite compounds with orthorhombic space group $Pnma$, where the incommensurate magnetic propagation vector $\mathbf{k} = (0,\ 0,\ k_z)$ is stable. Magnetic ions Fe1, Fe2, $R1$, and $R2$, all on $4c$ sites, form chains along the b direction. Due to strong antiferromagnetic intrachain Fe-Fe exchange interactions, each Fe chain adopts a collinear antiferromagnetic structure with a constant magnetic phase. The Fe chains are weakly coupled. Fe moments order with a collinear antiferromagnetic SDW below T_{N1} and a noncollinear low-symmetry cycloidal spiral magnetic structure below T_{N2}. The symmetry of the magnetic structures below T_{N2} allows the appearance of spin-induced ferroelectric polarization. At lower temperature, complex interplay of $3d$- and $4f$-electron sublattices leads to ordered Yb chains in $BaYbFeO_4$ below T_3 (stabilized by $4f-4f$ electron-exchange interactions), whereas, for $BaTmFeO_4$ below T_3, ordered Tm2 moments (induced by $3d-4f$ electron-exchange interactions) coexist with disordered Tm1 moments (due to frustration of magnetic exchange interactions).

ACKNOWLEDGMENTS

This work is partially based on experiments performed on HRPT diffractometer (Proposal No. 20202060) at the Swiss Spallation Neutron Source SINQ, Paul Scherrer Institute, Switzerland. This study was partly supported by JSPS KAKENHI Grants No. JP20H05276 and No. JP22H04601.

[1] E. Bousquet and A. Cano, Non-collinear magnetism in multiferroic perovskites, J. Phys.: Condens. Matter **28**, 123001 (2016).

[2] A. Kumar and S. M. Yusuf, The phenomenon of negative magnetization and its implications, Phys. Rep. **556**, 1 (2015).

[3] A. Dönni, V. Y. Pomjakushin, L. Zhang, K. Yamaura, and A. A. Belik, Origin of negative magnetization phenomena in $(Tm_{1-x}Mn_x)MnO_3$: A neutron diffraction study, Phys. Rev. B **101**, 054442 (2020).

[4] A. Dönni, V. Y. Pomjakushin, L. Zhang, K. Yamaura, and A. A. Belik, Magnetic properties and ferrimagnetic structures of Mn self-doped perovskite solid solutions $(Ho_{1-x}Mn_x)MnO_3$, J. Alloys Compd. **857**, 158230 (2021).

[5] T. Kimura, T. Goto, H. Shintani, K. Ishizaka, T. Arima, and Y. Tokura, Magnetic control of ferroelectric polarization, Nature (London) **426**, 55 (2003).

[6] S. W. Cheong and M. Mostovoy, Multiferroics: A magnetic twist for ferroelectricity, Nat. Mater. **6**, 13 (2007).

[7] A. A. Belik, N. Terada, Y. Katsuya, M. Tanaka, I. S. Glazkova, A. V. Sobolev, I. A. Presniakov, and K. Yamaura, Synthesis, structure, and magnetic and dielectric properties of magnetoelectric $BaDyFeO_4$ ferrite, J. Alloys Compd. **811**, 151963 (2019).

[8] A. A. Belik, A. Dönni, M. Tanaka, I. S. Glazkova, A. V. Sobolev, and I. A. Presniakov, Different magnetic and magnetodielectric behavior of Ba*R*FeO_4 ferrites with R = Ho, Er, Tm, and Yb, J. Alloys Compd. **922**, 166297 (2022).

[9] I. S. Glazkova, A. A. Belik, A. V. Sobolev, M. N. Smirnova, N. S. Ovanesyan, and I. A. Presniakov, Modulated magnetic structures in Ba*R*FeO_4 (R = Y and Dy): Magnetic and ^{57}Fe Mössbauer investigations, J. Phys. Chem. C **124**, 13374 (2020).

[10] F. Wrobel, M. C. Kemei, and S. Derakhshan, Antiferromagnetic spin correlations between corner-shared $[FeO_5]^{7-}$ and $[FeO_6]^{9-}$ units, in the novel iron-based compound: $BaYFeO_4$, Inorg. Chem. **52**, 2671 (2013).

[11] C. M. Thompson, J. E. Greedan, V. O. Garlea, R. Flacau, M. Tan, P. H. T. Nguyen, F. Wrobel, and S. Derakhshan, Partial spin ordering and complex magnetic structure in $BaYFeO_4$: A neutron diffraction and high temperature susceptibility study, Inorg. Chem. **53**, 1122 (2014).

[12] J. Z. Cong, S. P. Shen, Y. S. Chai, L. Q. Yan, D. S. Shang, S. G. Wang, and Y. Sun, Spin-driven multiferroics in $BaYFeO_4$, J. Appl. Phys. **117**, 174102 (2015).

[13] E. E. Gordon, S. Derakhshan, C. M. Thompson, and M. H. Whangbo, Spin-density wave as a superposition of two magnetic states of opposite chirality and its implications, Inorg. Chem. **57**, 9782 (2018).

[14] D. P. Kozlenko, N. T. Dang, R. P. Madhogaria, L. T. P. Thao, S. E. Kichanov, N. Tran, D. T. Khan, N. Truong-Tho, T. L. Phan, B. W. Lee, B. N. Savenko, A. V. Rutkaukas, L. H. Khiem, H. B. Nguyen, T. A. Tran, T. Kmjec, J. Kohout, V. Chlan, and M. H. Phan, Competing magnetic states in multiferroic $BaYFeO_4$: A high magnetic field study, Phys. Rev. Mater. **5**, 044407 (2021).

[15] C. H. Prashanth, T. W. Yen, A. Tiwari, P. Athira, S. M. Huang, B. R. Poojitha, D. P. Gulo, H. L. Liu, C. W. Wang, Y. K. Lin, Y. C. Chuang, Y. C. Lai, K. Jyothinagaram, H. D. Yang, and D. C. Kakarla, Interplay of magnetic and electric coupling across the spin density wave to conical magnetic ordering in a $BaHoFeO_4$ spin-cluster chain compound, J. Alloys Compd. **942**, 169017 (2023).

[16] P. Fischer, G. Frey, M. Koch, M. Könnecke, V. Pomjakushin, J. Schefer, R. Thut, N. Schlumpf, R. Bürge, U. Greuter, S. Bondt, and E. Berruyer, High-resolution powder diffractometer HRPT for thermal neutrons at SINQ, Phys. B: Condens. Matter **276–278**, 146 (2000).

[17] J. Rodriguez-Carvajal, Recent advances in magnetic structure determination by neutron powder diffraction, Physica B **192**, 55 (1993).

[18] V. Yu. Pomjakushin, D. V. Sheptyakov, K. Conder, E. V. Pomjakushina, and A. M. Balagurov, Effect of oxygen isotope substitution and crystal microstructure on magnetic ordering and phase separation in $(La_{1-y}Pr_y)_{0.7}Ca_{0.3}MnO_3$, Phys. Rev. B **75**, 054410 (2007).

[19] B. J. Campbell, H. T. Stokes, D. E. Tanner, and D. M. Hatch, ISODISPLACE: A web-based tool for exploring structural distortions, J. Appl. Crystallogr. **39**, 607 (2006); H. T. Stokes, D. M. Hatch, and B. J. Campbell, ISODISTORT, ISOTROPY Software Suite, iso.byu.edu.

[20] N. E. Brese and M. O'Keeffe, Bond-valence parameters for solids, Acta Crystallogr. B **47**, 192 (1991).

[21] See Supplemental Material at http://link.aps.org/supplemental/10.1103/PhysRevB.107.134412 for tables with selected bond lengths and interatomic distances, and figures with temperature dependence of magnetic susceptibility, refinements of neutron-diffraction patterns, and illustrations of magnetic structures for the compounds $BaYbFeO_4$ and $BaTmFeO_4$.

[22] K. Momma and F. Izumi, VESTA 3 for three-dimensional visualization of crystal, volumetric and morphology data, J. Appl. Crystallogr. **44**, 1272 (2011).

[23] A. H. Arkenbout, T. T. M. Palstra, T. Siegrist, and T. Kimura, Ferroelectricity in the cycloidal spiral magnetic phase of $MnWO_4$, Phys. Rev. B **74**, 184431 (2006).

[24] S. J. Luo and K. F. Wang, Multiferroicity in cycloidal spiral spin magnet β-$CrPO_4$, J. Alloys Compd. **726**, 833 (2017).

[25] R. A. Cowley, Structural phase transitions I. Landau theory, Adv. Phys. **29**, 1 (1980).

[26] H. Katsura, N. Nagaosa, and A. V. Balatsky, Spin Current and Magnetoelectric Effect in Noncollinear Magnets, Phys. Rev. Lett. **95**, 057205 (2005).

[27] S. Vilminot, M. Richard-Plouet, G. André, D. Swierczynski, M. Guillot, F. Bourée-Vigneron, and M. Drillon, Magnetic structure and properties of $Cu_3(OH)_4SO_4$ made of triple chains of spins $S = 1/2$, J. Solid State Chem. **170**, 255 (2003).

[28] S. Vilminot, G. André, F. Bourée-Vigneron, M. Richard-Plouet, and M. Kurmoo, Magnetic properties and magnetic structures of $Cu_3(OD)_4XO_4$, X = Se or S: Cycloidal versus collinear antiferromagnetic structure, Inorg. Chem. **46**, 10079 (2007).

[29] M. Hase, H. Kuroe, V. Yu. Pomjakushin, L. Keller, R. Tamura, N. Terada, Y. Matsushita, A. Dönni, and T. Sekine, Magnetic structure of the spin-1/2 frustrated quasi-one-dimensional antiferromagnet $Cu_3Mo_2O_9$: Appearance of a partially disordered state, Phys. Rev B **92**, 054425 (2015).

[30] M. Hase, A. Dönni, and V. Yu. Pomjakushin, Magnetic structures of nearly isostructural Tb_3RuO_7 and Nd_3RuO_7: Appearance of a partially disordered state only in the Tb compound, Phys. Rev B **104**, 214430 (2021).